Journal Name

ARTICLE

Electronic and Optical Properties of Narrow-band-emitting Red Nanophosphor K$_2$NaGaF$_6$:Mn^{4+} for Warm White Light-emitting Diodes

Chunyan Jiang,[a] Mikhail G Brik,[b,c,d] Lihua Li,[a] Liyi Li,[a] Jie Peng,[a] Maxim S. Molokeev,[e,f,g] and Mingying Peng*[a]

Recently, as a key red component in the development of warm white light-emitting diodes (WLEDs), Mn^{4+} doped fluorides with narrow red emission sparkle a rapidly growing interest as they improve the color rendition and enhance the visual energy efficiency. Herein, a red nanophosphor K$_2$NaGaF$_6$:Mn^{4+} with 150 - 250 nm in diameter has been synthesized by simple co-precipitation method. Rietveld refinement reveals that it crystallizes in space group Fm$\bar{3}$m with cell parameter a = 8.25320 (4). The exchange charge model (ECM) is used to calculate the energy levels of the Mn^{4+} ions in K$_2$NaGaF$_6$, which matches well with the experimental spectra. The as-synthesized phosphor exhibits narrow red emission at around 630 nm (spin-forbidden ^2E_g-$^4A_2$ transition of Mn^{4+} ions) when excited by 365 nm ($^4A_{2g}$ - $^4T_{1g}$) and 467 nm ($^4A_{2g}$ - $^4T_{2g}$), with a quantum efficiency (QE) of 61% and good resistance to thermal quenching. Based on the structure, the formation mechanism of ZPL is discussed. In addition, the concentration-dependent decay curves of Mn^{4+} in K$_2$NaGaF$_6$ are fitted by Inokuti-Hirayama model, suggesting that dipole-dipole interaction determines the concentration quenching. Finally, encouraged by the good performance, a warm LED with CRI of 89.4 and color temperature of 3779 K is fabricated by employing the tittle phosphor as a red component. Our findings suggest that K$_2$NaGaF$_6$:Mn^{4+} can be a viable candidate for red phosphor used in warm WLEDs.

1. Introduction

It is well known that energy saving is one of the fundamental ways to ease the contradiction between development and energy shortage. The phosphor-converted white light-emitting diode (pc-WLED) has been recognized as an energy efficient technological solution because of the advantages of energy-efficient, robust, long-lifetime and environmental friendliness.[1-3] Nowadays, the mainstream commercial pc-WLED has been based on blue chip and YAG: Ce^{3+} yellow phosphor. This combination provides a high conversion efficiency, close to the theoretical maximum. However, the lack of red emission leads to cool white light with low color rendering index (CRI, < 80) and high correlated color temperature (CCT > 4500 K), which contradicts to the new metric in the field of illumination-grade lighting focusing on high luminous and brilliant color rendering

properties.[4] In order to compensate the red light deficiency in emission spectrum, many efforts have been devoted to the development of red phosphors. Among them, the Eu^{2+} doped nitrides have been shown to be the most promising red-emitting phosphor. It possesses excellent luminescence properties, good thermal stability and chemical stability.[5-7] Nevertheless, some drawbacks such as harsh synthesis condition (usually high temperature, high pressure, and oxygen/water free), quantum loss resulted from re-absorption and the decreased energy efficiency due to insensitive deep red emission (> 650 nm) still seriously hinder its wider commercialization. In this regard, how to further improve color rendition of pc-WLEDs without losing excess energy efficiency still remains a great challenge. To solve this problem, one effective approach is to develop narrow-band red-emitting phosphors with emission spectrum adapted to the visual sensitivity of human eye.[8,9]

The Mn^{4+} ions have the 3d^3 electron configuration and are, usually stabilized at the octahedral sites. When doped in fluoride, Mn^{4+} exhibits broad excitation located at 360, 460 nm, and narrow emission band at 630 nm, which can well satisfy the above requirements (sensitive red emission, no reabsorption). In addition to superior optical luminescence properties, Mn^{4+} doped fluorides are also thermally stable, and can be synthesized in a convenient way, thus attracting a rapidly growing interest as red phosphors for white LEDs.[10] In 2014, Liu and Chen's group reported a highly efficient red-emitting phosphor based on K$_2$TiF$_6$:Mn^{4+}, which exhibits emission peaks at 608, 612, 630, 634 and 646 nm when excited at maximum absorption peak 460 nm.[11] By employing it as a red phosphor, a high performance white LED with low correlated color

temperature (3556 K), high color render index (CRI = 81) and luminous efficiency of 116 lm W^{-1} was fabricated. Immediately after that, many groups reported the synthesis and performance of Mn^{4+} doped fluorides red phosphor for warm WLEDs. Most works focused on A_2BF_6:Mn^{4+} (A = K$^+$, Na$^+$, Cs$^+$, Rb$^+$, NH$_4^+$; B = Ge^{4+}, Ti^{4+}, Si^{4+}, Zr^{4+}, Sn^{4+}) and $BaMF_6$:Mn^{4+} (M = Ge^{4+}, Ti^{4+}, Si^{4+}).[12-18] Some of them with high luminous efficiency suggested promising applications in warm WLEDs;[12] and some with low symmetry featuring strong ZPL emission were proposed to further improve the CRI of WLEDs.[14] Nevertheless, in all of them, Mn^{4+} are incorporated into the cation sites with same valence. Due to the similar ion radius between Mn^{4+} and Al^{3+} (Ga^{3+}), it is strongly believable that the Mn^{4+} can also been doped into Al and Ga site in fluoroaluminate and fluorogallate via non-equivalent substitution just like Mn^{4+} doped oxide ($Sr_4Al_{14}O_{25}$:Mn^{4+}, $Mg_3Ga_2GeO_8$:Mn^{4+}).[19,20] And yet, there are relatively few studies devoted to them.[21-23]

Elpasolites A_2BXF_6 (A = Na$^+$, K$^+$, Cs$^+$, Rb$^+$, B = Li$^+$, Na$^+$, K$^+$, X = Al^{3+}, Ga^{3+}) have various forms due to different cation combinations.[24] They possess stiff lattices with a band gap of > 5 eV. Emissions are reported in UV region when doped with rare earth ions such as Ce^{3+} and Eu^{2+} in these materials.[25] As this structure consists of isolated AlF$_6$ or GaF$_6$ octahedrons, elpasolites are regarded as suitable hosts for Mn^{4+} doping. In this work, we report a novel red nanophosphor K_2NaGaF_6:Mn^{4+} synthesized by a simple co-precipitation method for the first time. The crystal structure, morphology and composition of samples are investigated in detail by XRD, Rietveld refinement, SEM and TEM. The luminescence properties including diffuse reflection spectra, quantum yield, static and dynamic photoluminescence, concentration and temperature dependent spectra are studied systematically. Thereafter, as a concept evaluation, the tittle phosphor is employed as a red component to fabricate warm WLED, and the performance of LED under different drive currents is evaluated. The results show that K_2NaGaF_6:Mn^{4+} has promising application potential in warm WLEDs.

2. Experiment and Characterization

2.1 Materials
KF (99.99%), NaF (99.99%), Ga(NO$_3$)$_3$ (99.99%), HF (48 wt %), KHF$_2$ (99.9%) were purchased from Aladdin Reagents. KMnO$_4$ (99.5%), acetone (AR), H$_2$O$_2$ (30 wt %) were obtained from Guangzhou Chemical Reagent Factory.

2.2 Preparation
The preparation of K$_2$MnF$_6$
K_2MnF_6 precursor was prepared according to the technique described elsewhere.[26] KMnO$_4$ (1.5 g) and KHF$_2$ (30 g) were weighed and dissolved in 100 ml HF. After stirring for 30 min, the solution was put in an ice bath. Then 0.3 ml H$_2$O$_2$ was added drop by drop, meanwhile the color of the solution turn from purple to brown, and a yellow precipitate was obtained. The K$_2$MnF$_6$ precipitate was separated by centrifugation, washed several times by acetone, and then dried at 70 °C for 3h.

The preparation of K$_2$NaGaF$_6$:Mn^{4+}
The K_2NaGaF_6:Mn^{4+} phosphor was prepared by a simple co-precipitation method. Take K_2NaGaF_6:3% Mn^{4+} for example. K_2MnF_6 (0.1483 g) was weighed and dissolved in 10 ml HF, after vigorous

stirring for 5 min, Ga(NO$_3$)$_3$ (5.1148 g) was added. Thereafter solution of salts of remaining metals NaF (0.8389 g) and KF (2.3239 g) were added, the solution was kept stirring for further 20 min. Finally, the precipitate was separated by centrifugation, washed several times by acetone, and then dried at 70 °C for 3h.

2.3 Characterization
The phase purity of the samples was checked by X-ray diffraction using a D8 ADVANCE X-ray diffractometer with Cu Kα radiation (λ= 0.15418 nm) at 40 kV and 40 mA. The powder diffraction data of K_2NaGaF_6 for Rietveld analysis was collected at room temperature with a Bruker D8 ADVANCE powder diffractometer (Cu-Kα radiation) and linear VANTEC detector, the step size of 2θ was 0.013°, counting time was 1 s per step. The Rietveld refinement was performed by using TOPAS 4.2.[27] The high-resolution transmission electron microscopic (HRTEM) images were recorded with a JEOL JEM-2100 electron microscope operating at 200 kV. The scanning electron micrograph (SEM) and elemental composition were obtained using a FEI Nova NanoSEM403 scanning electron microscope equipped with energy dispersive X-ray spectrometry (EDS) from Brucker. The diffuse reflection spectra were recorded using a Cary 5000 UV-vis-NIR spectrophotometer equipped with a double out of Plane Littrow monochromator using BaSO$_4$ powder as a standard reference. The static and dynamic spectra in UV-visible range at room temperature were measured with Edinburgh FLS 920 spectrometer equipped with a red-sensitive photomultiplier (Hamamatsu R928P), 450W xenon lamp and 60 W μF flash lamp with a pulse width of 1.5 - 3.0 μs and pulse repetition of 40 kHz. Absolute quantum yield was measured by the standard spectrometer (C11347-11, Hamamatsu Photonics K. K.). The temperature-dependent (25−300 °C) PL spectra were detected on Edinburgh FLS 920 spectrometer equipped with a temperature controller. The color rendering index (CRI) and correlated color temperature (CCT) as well as Commission International de l'Eclairage (CIE) chromaticity were evaluated by a photoelectricity test system (V2.00 LED spec system).

3. Calculation Details

The electronic properties of the host were studied using the CASTEP module of Materials Studio.[28] The exchange-correlation functionals were represented by the generalized gradient approximation (GGA) and local density approximation (LDA).[29-31] The plane-wave basis energy cut-off was chosen as 410 eV; the ultrasoft pseudopotentials were used in all calculations. The convergence parameters were as follows: total energy tolerance 5×10^{-6} eV/atom, maximum force tolerance 0.01 eV/Å, maximum stress component 0.02 GPa, and maximum displacement 5×10-4 Å. The k-points grid was chosen as 10×10×10. The electronic configurations were 3s^{2}3p^{6}4s^1 for K, 2s^{2}2p^{6}3s^1 for Na, 3d^{10}4s^{2}4p^1 for Ga, and 2s^{2}2p^5 for F, correspondingly.

As the next step to study the electronic and optical properties of the doped material, the exchange charge model (ECM) was used to calculate the energy levels of the Mn^{4+} ions in K_2NaGaF_6.[32] All relevant details of the ECM, including the equations used, their explanations and calculations procedure, have been described at length before (e.g.[32,33,34] and references therein), so they are not repeated here for the sake of brevity. Successful calculations of the energy level schemes of the transition metal and rare earth ions
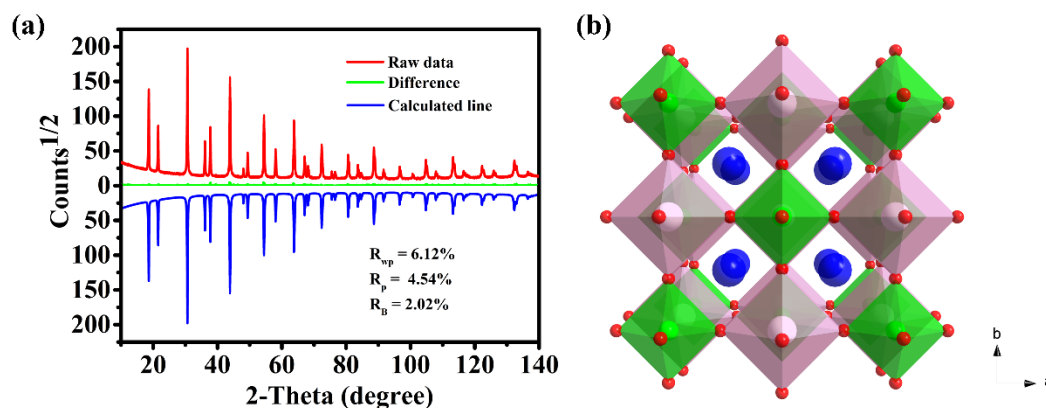
Fig. 1 (a) Experimental (red line) and calculated (blue line) XRD patterns and their difference (green line) for K_2NaGaF_6. (b) The structure of K_2NaGaF_6 viewed along the c axis. Blue, white, green, red sphere balls represents K, Na, Ga, F atom, respectively.

prove the reliability of the ECM. The crystal structure data on K_2NaGaF_6 are determined in the present work. After doping, the Mn^{4+} ions occupy the Ga positions, which are 6-fold coordinated by the fluorine ions. A cluster consisting of 78199 ions was used to calculate the crystal lattice sums.

4. Results and Discussion

4.1 Crystal structure, Morphology and Composition Analysis

Rietveld refinement was carried out through TOPAS software to identify the phase and crystal structure of the as-prepared K_2NaGaF_6 compound. As all peaks were well indexed by cubic cell ($Fm\overline{3}m$) with parameters close to K_2NaCuF_6 (elpasolite-type structure),[35] crystal structure of K_2NaCuF_6 was taken as starting model for Rietveld refinement. Fig 1a displays the Rietveld refinement pattern for K_2NaGaF_6. The experimental, calculated, and difference results of the XRD refinement of K_2NaGaF_6 are depicted by red, blue and green lines. The goodness of fit parameters R_{wp} = 6.12%, R_p = 4.54%, R_B = 2.02% implies the phase purity of K_2NaGaF_6. The corresponding structure parameters as a result of refinement are shown in Table 1. The compound K_2NaGaF_6 crystallizes in a cubic structure with the space group $Fm\overline{3}m$, and its lattice parameter is fitted to be a = 8.25320 (4) and the unit cell volume V = 562.169 (7) $Å^3$. The crystal structure of K_2NaGaF_6 as viewed along the c-axis is shown in Fig 1b, the compound is built up by co-vertex connected GaF_6 and NaF_6 octahedrons with the K atoms occupy the 12-coordinated cavities. Given the similar ionic radii between Ga^{3+} (r = 0.62 Å, CN = 6) and

Mn^{4+} (r = 0.52 Å, CN = 6) in six-fold coordination, Mn^{4+} is doped into the Ga^{3+} sites in K_2NaGaF_6.

Fig 2a presents the XRD patterns of $K_2NaGa_{1-x}F_6$:xMn^{4+} (x=0.3%, 1.0%, 3.0%, 5.0%, 7.0%). The simulated XRD pattern of refined K_2NaGaF_6 is shown at the bottom as a reference. The XRD patterns of all Mn^{4+} doped K_2NaGaF_6 samples are similar and can be well indexed with the refined result of K_2NaGaF_6, indicating that all the Mn^{4+} doped K_2NaGaF_6 samples are of a pure phase, and Mn^{4+} dopants has no obvious influence on the structure of K_2NaGaF_6. Meanwhile, the diffraction peaks shift slightly to the higher angle side with the increase of Mn^{4+} concentration in $K_2NaGa_{1-x}F_6$:xMn^{4+}, as shown in Fig 2b. This observation illustrates that the Mn^{4+} is successfully incorporated into Ga^{3+} site in K_2NaGaF_6 with the decrease of interplanar spacing d value, as the radius of Mn^{4+} is smaller than Ga^{3+}.
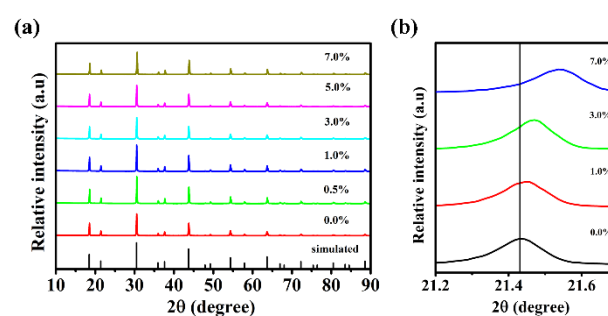

Fig. 2 (a) XRD patterns of $K_2NaGa_{1-x}Mn_xF_6$ (x = 0, 0.5, 1.0, 3.0, 5.0, 7.0%). (b) Peak shifts of the series of XRD patterns.

Table 1. Refined structure parameters of the K_2NaGaF_6 sample.

Atom	Site	x	y	z	occ	biso (A2)
K	8c	1/4	1/4	1/4	1	1.66 (2)
Na	4b	1/2	1/2	1/2	1	1.22 (3)
Ga	4a	0	0	0	1	0.77 (2)
F	24e	0.2285 (1)	0	0	1	1.76 (2)

[a] Symmetry, cubic; space group, $Fm\overline{3}m$; a = 8.25320 (4), V = 562.169 (7) $Å^3$.
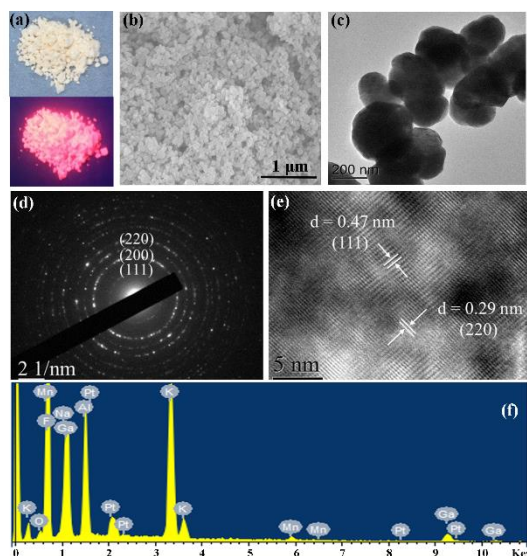
Fig. 3 (a) Photographs of K_2NaGaF_6:3% Mn^{4+} sample under fluorescent lamp (top) and 365 nm UV lamp (down). (b) SEM image (c) TEM image, (d) SAED pattern, (e) HRTEM image and (f) EDS analysis of K_2NaGaF_6:3% Mn^{4+} sample.

The as-synthesized phosphor presents a light yellow color powder in Fig 3a, and when exposed to 365 nm UV light, the phosphor appears intense red light. To further confirm the structure and morphology of K_2NaGaF_6: Mn^{4+}, HRTEM and SEM were employed. The SEM (Fig 3b) and low-magnification TEM images (Fig 3c) clearly show that the as-prepared K_2NaGaF_6:Mn^{4+} sample is sphere-like with 150 - 250 nm in diameter. The EDS analysis in Fig 3f demontrates that the sample is composed of K, Na, Mn, Ga, F, a weak Mn signal is due to its relative low content, and the singal of Al and Pt originates from the aluminum supptor and conductive layer in sample pretreatment. The atom ratio (2:1:1:6) of K, Na, Ga, F calculated from the EDS analysis is in good accordance with the formula K_2NaGaF_6, which further illustrates the phase purity of the as-prepared sample. Fig 3e displays the high resolution transmission electron microscopy (HRTEM) image, lattice distance of 0.47 nm and 0.29 nm match well with the (111) and (220) crystal plane of K_2NaGaF_6. The legible lattice distance in HRTEM image and typical SAED pattern (Fig 3d) together indicate the good crystallization of the K_2NaGaF_6:Mn^{4+} samples.

4.2 Photoluminescence Properties
4.2.1 Electronic Structure and Optical Bandgap

The electronic properties of the host were studied using the CASTEP module of Materials Studio. The optimized lattice constant (8.4021 Å, GGA, and 8.0311 Å, LDA) is close to the corresponding experimental value of 8.2532 Å. The electronic band structure is shown in Fig 4a. The bandgap is direct, and the calculated band gaps of K_2NaGaF_6 are 5.925 eV (GGA) and 6.473 eV (LDA), respectively. Such wide electronic band gaps favor doping with impurity ions (Mn^{4+} in particular), since such a wide band gap ensures location of the impurity energy levels in the host band gap. The origin of the electronic bands can be understood with the help of the density of states (DOS) diagrams shown in Fig. 4b. The conduction band (whose states exhibit well-pronounced dispersion) consists of the s and p states of K, Na and Ga. The valence band stretches from about -5 eV to 0 and is dominated by the F 2p states. There are several narrow deep bands at -10 eV (K 3p and Ga 3d states), -20 eV (F 2s and Na 2p states), -26 eV (K 3s states) and -47 eV (Na 2s states).

To verify the bandgap experimentally, the diffuse reflection spectra of K_2NaGaF_6 host and K_2NaGaF_6:Mn^{4+} are depicted in Fig 5a. For K_2NaGaF_6 host, the diffuse reflection spectrum shows a plateau of high reflection in the wavelength range of 250 - 800 nm, then dramatically decrease from 250 - 200 nm. The absorption near 200 nm is attributed to the host absorption band. First, to determine K_2NaGaF_6 is a direct-gap material or not. The plot $[F(R\infty)hv]^2$ versus (hv-Eg) is calculated from the absorption spectrum, where hv is the photo energy; [36] Eg is the optical bandgap energy; $F(R\infty)$ is a Kubelka-Munk function defined as:[37]

$$F\left(R\infty\right)=\left(1-R\infty\right)^2/\left(2R\infty\right) \tag{1}$$

Where $R\infty$ denotes the reflectivity. The plot is shown in the bottom inset of Fig 5a, a linear dependence is observed, indicating the fact that the K_2NaGaF_6 is a direct band gap material, in agreement with our calculations. Then, by extrapolating the linear dependence to zero, the optical bandgap of K_2NaGaF_6 is obtained as Eg = 5.49 eV, which agrees well with the calculated value 5.925 eV (GGA), and also
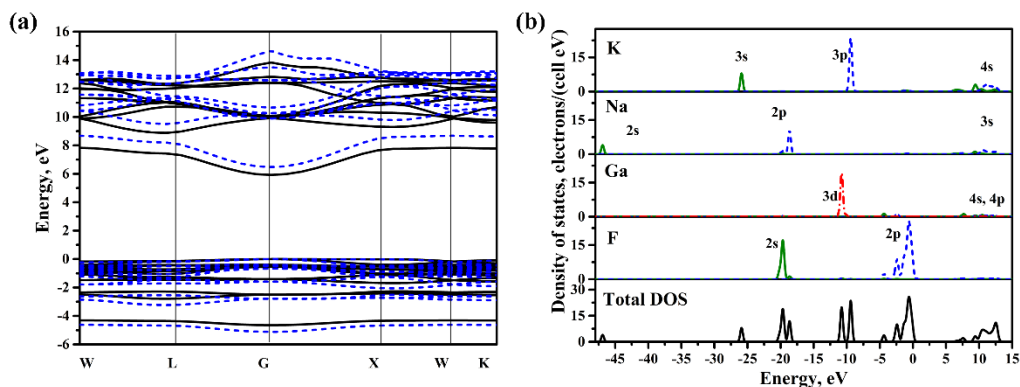

Fig. 4 (a) Calculated band structure (solid line and dashed line present the results of GGA and LDA, respectively) for K_2NaGaF_6. (b) Density of states (DOS) diagram for K_2NaGaF_6 (Green solid line, blue dashed line and red dashed line represents s, p and d state, respectively).
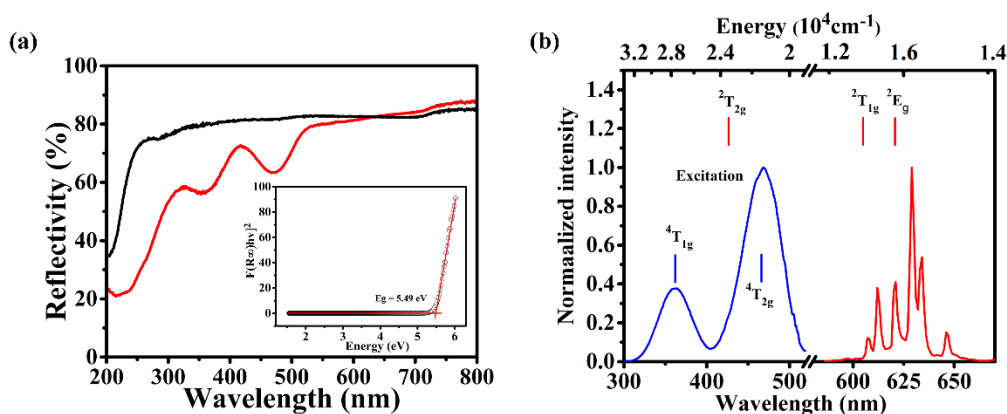
Fig. 5 (a) Diffuse reflection spectra of K_2NaGaF_6 host (black line) and K_2NaGaF_6:Mn^{4+} (red line) at RT, bottom inset is a plot of $[F(R\infty)h\nu]^2$ versus energy (eV). (b) Comparison between the calculated energy levels of Mn^{4+} (vertical lines) and experimental excitation/emission spectra (solid lines) of K_2NaGaF_6:Mn^{4+}.

comparable with that of other fluorides.[38,39] While, for Mn^{4+} doped K_2NaGaF_6, except the absorption near 200 nm, there are another two evident broad absorption in 415 nm - 525 nm and 323 nm - 410 nm, whose origin will be discussed later. Notably, strong absorption locates at blue region, which enables the phosphor a perfect match with blue chip.

4.2.2 Crystal Field Calculations and Spectroscopic Data

The exchange charge model (ECM) was used to calculate the energy levels of the Mn^{4+} ions in K_2NaGaF_6. The K_2NaGaF_6 crystallizes in the $Fm\bar{3}m$ space group (No. 225) with the lattice constant a=8.2532 Å. After doping, the Mn^{4+} ions occupy the Ga^{3+} positions, which are 6-fold coordinated by the fluorine ions at the distance of 1.8856 Å, forming an ideal octahedron. Due to the ideal octahedral symmetry, only two crystal field parameters are not zero. Their values (in cm^{-1}, Stevens normalization) are: $B_4^0 = 5598$, $B_4^4 = 27990$. The values of the Rach parameters B and C, which were chosen from the best agreement with experimental data, are B=595 cm^{-1}, C=3837 cm^{-1}. The calculated energy levels of Mn^{4+} ions in K_2NaGaF_6 are collected in Table 2, whereas Fig 5b visualizes good agreement between the calculated energy levels and experimental excitation/emission spectra. In the photoluminescence excitation spectra, the two broad excitation band centered at 365 nm and 467nm in the range of 300-

515 nm, with full width at half maxima of 47 nm and 53 nm, which are coincident with that in Fig 5a, are assigned to the spin-allowed $^4A_2$-$^4T_1$ and $^4A_2$-$^4T_2$ transitions, respectively. In the photoluminescence emission spectra, there are several sharp lines in the range of 580-660 nm, originating from the transition of ^2E -$^4A_2$. For Mn^{4+}, the emission transition ^2E -$^4A_2$ is spin-forbidden, the vibronic modes usually couple with electronic transition. The band at 621 nm is ascribed to the zero-phonon line (ZPL); the bands at 646, 634 and 629 nm is attributed to stokes electronic transitions coupled with the ν_6, ν_4, ν_3 vibronic modes, respectively; and the bands at 612, 606 and 598 nm is due to anti-stokes electronic transitions coupled with the ν_6, ν_4, ν_3 vibronic modes, respectively. A distinct feature of the obtained emission spectra is a high intensity of the ZPL. As referring to the relationship between the ZPL and symmetry, the symmetry of Ga site is demonstrated to be O_h from structure analysis, and there should be no ZPL. But, considering the unequal valence state and different ion radius in Ga^{3+} and Mn^{4+}, the lattice can be partially distorted after doping. This partial site symmetry decrease caused by distortion may explain the strong ZPL in K_2NaGaF_6:Mn^{4+}, and similar phenomenon take places in other Mn^{4+} doped high symmetry fluoroaluminates.[21,40]

4.2.3 Doping Concentration-dependent Luminescence

To check the relationship between PL intensity and different doping concentrations, the emission spectra of $K_2NaGa_{1-x}F_6$:xMn^{4+} at different x values (x = 0.5%, 1%, 3%, 5%, 7%) are depicted in Fig 6a. Under 467 nm excitation, the emission intensity of K_2NaGaF_6:Mn^{4+} firstly rises with the increase of the doping concentration and reaches a maximum when the Mn^{4+} concentration is 3%, then goes down with further increasing doping concentration, as clearly described in Fig 6d. The critical concentration is 3% in this system. For comparison, Fig 6b presents the emission spectra of K_2NaGaF_6:Mn^{4+} with different doping concentrations that have been normalized to highest intensity, the contour of spectra maintain unchanged except the ZPL. The relative change of the ZPL intensity is described in Fig 6b, the ZPL intensity increases with the doping concentration. This fact further prove that the ZPL derived from the lattice distortion after Mn^{4+} doped into Ga^{3+}.

On the other hand, Fig 6c presents the decay curves of 621 nm emission of K_2NaGaF_6:Mn^{4+} upon 465 nm excitation with changing

Table 2. Calculated energy levels (in cm^{-1}) of Mn^{4+} ions in K_2NaGaF_6.

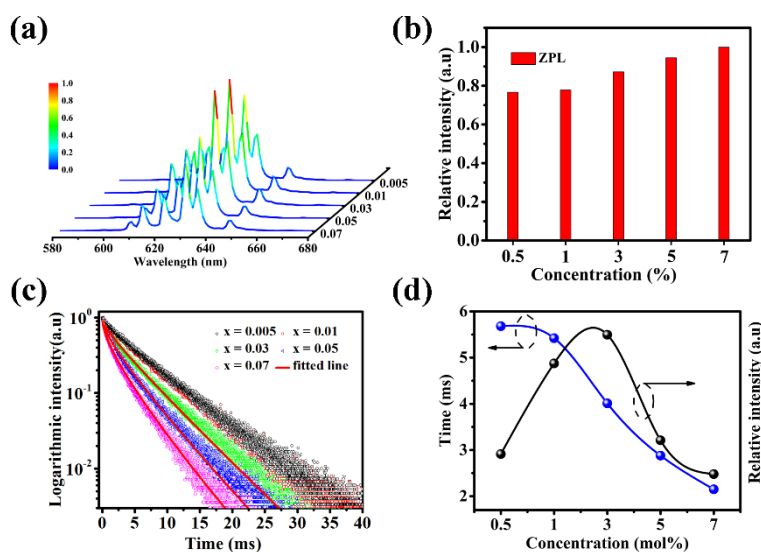| Energy levels, Oh group notation	K_2NaGaF_6:Mn^{4+}
$^4A_{2g}$ (^4F)	0
^2E_g (^2G)	16104
$^2T_{1g}$ (^2G)	16539
$^4T_{2g}$ (^4F)	21325
$^2T_{2g}$ (^2G)	24522
$^4T_{1g}$ (^4F)	27703
$^2A_{1g}$ (^2G)	35216
$^2T_{2g}$ (^2H)	37224
$^4T_{1g}$ (^4P)	45196

Fig. 6 (a) Emission spectra of $K_2NaGa_{1-x}F_6$:xMn^{4+} (x = 0.5%, 1%, 3%, 5%, 7%) under 467 nm excitation. (b) Relative ZPL intensity in normalized emission spectra of K_2NaGaF_6:Mn^{4+} as a function of doping concentration. (c) Decay curves of 621nm emission in $K_2NaGa_{1-x}F_6$:xMn^{4+} (x = 0.5%, 1%, 3%, 5%, 7%) under the excitation of 467 nm. (d) Concentration dependence of lifetime and relative integrated intensity for K_2NaGaF_6:Mn^{4+}.

Mn^{4+} concentration, and the lifetimes are collected in Fig 6d. For low concentration of Mn^{4+} (x = 0.5%), the decay curve is nearly single exponential, and the emission intensity y after t s decay can be written as

$$y = y_0 \exp\left[-\left(\frac{t}{\tau}\right)\right]$$

(2)

Where τ is the intrinsic lifetime, y_0 presents the initial intensity, t is the time. The intrinsic lifetimes of Mn^{4+} (x = 0.5%, 1.0%) is fitted to be 5.68 ms, which is similar to that of Mn^{4+} in another host.[41] While for higher concentration of Mn^{4+} (x = 1.0%, 3.0%, 5.0%, 7.0%), the decay curves gradually deviate from single exponential and the lifetimes are shorten, indicating an extra decay channel is active. With the increase of concentration, the Mn^{4+}-Mn^{4+} energy transfer becomes more efficient. The excitation energy migrates over and depletes in a quenching center. Therefore, the lifetime decreases as non-radiative energy migrates.[42] To assume the nature of interaction process under critical concentration, Inokuti-Hirayama model is introduced to investigate the shape of decay curves for different multipolar interactions.[43]

$$I(t)=I(0)\exp\left[-\left(\frac{t}{\tau}\right)-\frac{4\pi}{3}\Gamma\left(1-\frac{3}{s}\right)C_A C_{DA}{}^{3/s}t^{3/s}\right]$$

(3)

Where I(0) is the initial emission intensity, t is the time after excitation, τ is the intrinsic lifetime of Mn^{4+}, Γ( ) is a gamma function, C_A is the concentration of Mn^{4+}, C_{DA} is the energy transfer micro-parameter, s stands for the specific multipolar interaction, 6, 8,10 for the dipole-dipole, dipole-quadrupole, quadrupole-quadrupole interactions, respectively. When s is set to 6, the best fitting can be achieved as shown in Fig 6c, suggesting that dipole-dipole is the main interaction in the energy transfer process. According to the fitting results, the average C_{DA} is 5.5946×10^{-45} m^6 s^{-1}.

As for luminescence, quantum yield is an important parameter

of phosphor and determines its performance directly. The inner quantum yield is defined by:[44]

$$\eta_{in} = \frac{\int L_S}{\int E_R - \int E_S}$$

(4)

Where L_S denotes the emission intensity of sample, E_R and E_S represents the intensities of the excitation light not absorbed by the reference and sample, respectively. Based on above equation, quantum yield of the optimum concentration sample $K_2NaGa_{0.97}F_6$:$3\%Mn^{4+}$ is determined to be 61%.

4.3 Thermal Stability

For a phosphor, thermal stability is another essential aspect when evaluating the performance of LED as it changes the color coordinates and lowers the luminous efficiency. Fig 7a shows the temperature-dependent emission spectra of the optimum concentration sample $K_2NaGa_{0.97}F_6$:$3\%Mn^{4+}$ under 467 nm excitation. Obviously, the emission intensity drops continuously with the increase of temperature, and the relative intensities at different temperatures are shown in Fig 7b. When the temperature reaches 150 °C, the emission intensity drops to 71.9% of the initial PL intensity. To further go into the dynamics of the Mn^{4+} luminescence process, the emission spectra are normalized to highest intensity in Fig 7c. With the increase of temperature, the relative ZPL intensity decreases while the anti-stokes intensity increases. This means that the ZPL emission competes with anti-stokes emission in the radiative process.[14] As the temperature increases, the excited electron tends to populate higher vibration levels. Hence, the anti-stokes emission with an emission energy higher than ZPL transition is more likely to happen than the ZPL emission. On the other hand, decay curves of 621 nm emission in $K_2NaGa_{0.97}F_6$:$3\%Mn^{4+}$ under different temperatures are also investigated and depicted in Fig 7d. The decay goes faster with the increasing temperature. As can be seen in Fig 7b,
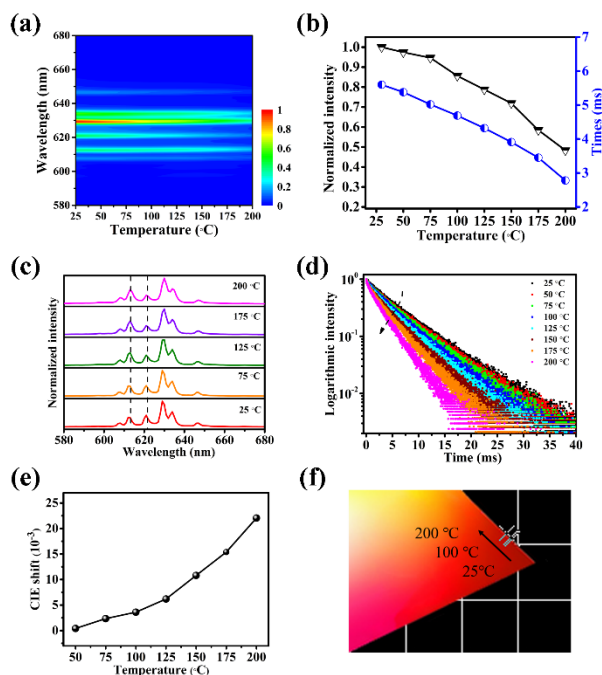
Fig. 7 (a) Emission spectra, (b) integrated emission intensity, lifetime and (c) highest height-normalized emission spectra of $K_2NaGa_{0.97}F_6$:3%Mn^{4+} at different temperatures. (d) Temperature-dependent decay curves of 626 nm emission of $K_2NaGa_{1-x}F_6$:3%Mn^{4+} under the excitation of 467 nm. (e) Chromaticity shift and (f) CIE chromaticity coordinate of $K_2NaGa_{1x}F_6$:3%Mn^{4+} as a function of temperature.

the lifetime drops from 5.60 ms to 2.78 ms from 25 °C to 200 °C. Apparently, both lifetime and luminescence decrease illustrate the thermal quenching in $K_2NaGa_{0.97}F_6$:3%Mn^{4+}. And the probability of thermal quenching is strong related to the activation energy, systematic studies have shown that the emission intensity decreases exponentially with the activation energy, their relationship can be expressed as:[45]

$$\frac{I(T)}{I_0} = \left[1 + A\exp\left(-\frac{\Delta E}{k_B T}\right)\right]^{-1}$$

(5)

Where I_0 is the initial emission intensity, I(T) is the intensity at temperature T, ΔE is the activation energy, A is a constant, k_B is Boltzmann's constant. The ΔE is fitted to be 0.324 eV, which is relative high when compared with that of other Mn^{4+} doped phosphors.[46,47]

Except for the thermal quenching behavior, the chromaticity stability was also studied. Fig 7f presents the changes of CIE chromaticity coordinates of $K_2NaGa_{0.97}F_6$:3%Mn^{4+} at different temperatures. The chromaticity coordinates shift from (0.6901, 0.3098) to (0.6806, 0.3192) with the temperature rising from room temperature to 200 °C. Furthermore, to quantify the variations, the chromaticity shifts (ΔE) are calculated based on the following equation:

$$\Delta E = \sqrt{\left(u_t{'} - u_0{'}\right)^2 + \left(v_t{'} - v_0{'}\right)^2 + \left(w_t{'} - w_0{'}\right)^2}$$

(6)

Where u' = 4x/(3-2x+12y), v' = 9y/(3-2x+12y), w' = 1- u'- v'. u', v' and w' are the chromaticity coordinates in uniform color space 1976, x

and y are the chromaticity coordinates in CIE 1931. $u_t{'}$ and $u_0{'}$ stands for the chromaticity coordinates u at 25 °C and given high temperature, respectively. The calculated CIE shifts of $K_2NaGa_{0.97}F_6$:3%Mn^{4+} under the temperature range from 50 °C to 200 °C are plotted in Fig 7e. The chromaticity shift is 10.8×10^{-3} at 150 °C, and 22.0×10^{-3} at 200 °C. By contrast, the chromaticity shift of $CaAlSiN_3$:Eu^{2+} is 25.6×10^{-3} at 150 °C, 39.2×10^{-3} at 200 °C.[48] This result indicates the chromaticity stability in K_2NaGaF_6: Mn^{4+} is superior to the commercial red phosphor $CaAlSiN_3$:Eu^{2+}.

4.4 Application in WLEDs

Given the appropriate optical properties, the potential application of the as-prepared phosphor in WLEDs is further evaluated. A series of LED (LED I - LED III) are fabricated by the method of "blue chip + commercial yellow phosphor $Y_3Al_5O_{12}$:Ce^{3+} + different amounts of tittle red phosphor K_2NaGaF_6:3%Mn^{4+}". Fig 8a, b, c presents the electroluminescence spectra of the as-fabricated LEDs and according photographs at a drive current of 20 mA. It is obvious that the red region increases markedly with increasing the content of K_2NaGaF_6:3%Mn^{4+}. The color coordinate of LEDs moves gradually to the warm white region in the CIE 1931 color spaces, as shown in Fig 8d. Table 3 shows the performance test of LED devices, Due to the addition of red phosphor K_2NaGaF_6:3%Mn^{4+}, the color render index of LED is effectively improved from 75.9, 80 to 89.4, and the color temperature changes from 4496 K, 4132 K to 3779 K. For optimum LED III, the CIE color coordinate lies near at black body locus, the luminous efficiency is 84.37 lm/W. The corresponding devices emit bright warm light as shown in the inset of Fig 8c. These inspiring results indicate that the red phosphor K_2NaGaF_6:Mn^{4+} may potentially be used in warm WLEDs.

Furthermore, the effect of drive current on the performance of LED III is measured. Fig 9a presents the electroluminescence spectra of LED III under different drive currents. As can be seen, the emission intensity enhances gradually with increasing drive current and no saturation phenomenon is detected. In addition, the shape of emission spectra changes little with the drive current, thus the LED III undergoes slight color temperature, CRI and color coordinates shifts as seen in Fig 9c, d. When the drive current increases from 20 to 350 mA, the color temperature increases from 3779 K to 4304 K,
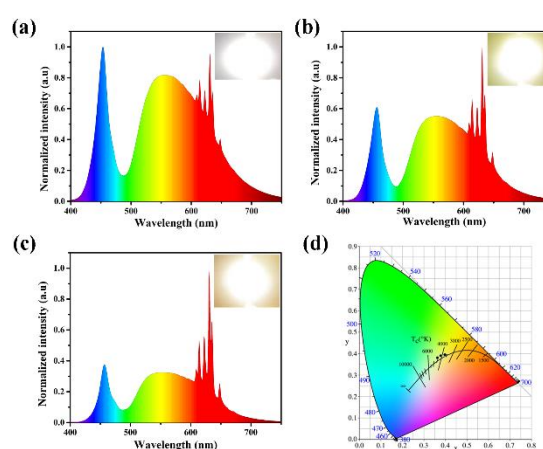

Fig. 8 (a, b, c) Electroluminescence (EL) spectra (d) and the CIE chromaticity diagram of WLED fabricated with different K_2NaGaF_6 /YAG:Ce^{3+} ratio under 20 mA drive current.

Table. 3 Chromaticity coordinates and performance parameter of the fabricated WLEDs.

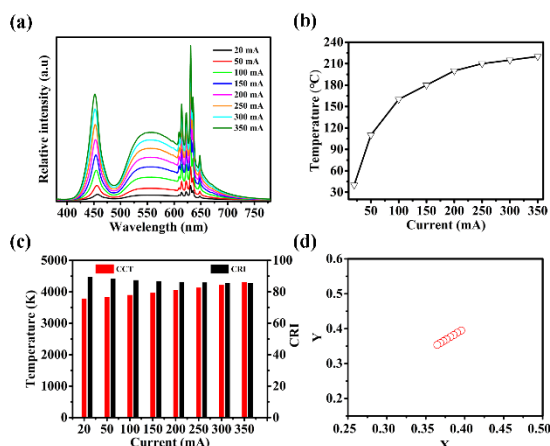| No	YAG:KNGF (weight ratio)	Current (mA)	CCT (K)	CRI	Chromaticity coordinate		Luminous efficiency (lm/W)
					x	y	
I	1:5	20	4496	75.9	0.3640	0.3812	110.59
II	1:7	20	4132	80.0	0.3785	0.3911	94.32
III	1:9	20	3779	89.4	0.3967	0.3937	84.37

Fig. 9 (a) Electroluminescence (EL) spectra, (b) junction temperature, (c) correlated color temperature, color render index (d) and color coordinates of LED III under different drive currents.

while the CRI decreases from 89.4 to 85.5. Most importantly, the practical junction temperature of LED is also estimated and exhibited in Fig 9b. It gives the information that for high power LED device, the junction temperature usually exceeds 50 °C, and it increases with the increasing drive current. When the drive current is 350 mA, the junction temperature can even reach to 210 °C. Therefore, the evaluation of thermal stability in phosphor is rather necessary.

5. Conclusion

In summary, a novel red nanophosphor K_2NaGaF_6:Mn^{4+} has been synthesized by simple co-precipitate method. The phase purity is confirmed by XRD and Rietveld refinement. The SEM and TEM analysis reveal that the phosphor is 200 nm in diameter with high crystallinity. The energy levels of the Mn^{4+} ions in K_2NaGaF_6 are calculated using the ECM method of crystal field theory and allow for the assignment of spectra. The phosphor K_2NaGaF_6:Mn^{4+} exhibits narrow red luminescence at around 630 nm when excited by 365 and 467 nm, with a quantum yield of 61%. The ZPL appears due to partial lattice distortion after doping. For K_2NaGaF_6:Mn^{4+}, the optimum concentration is determined to be 3%, and efficient energy transfer dominated by dipole–dipole interaction is implied to be responsible for the concentration quenching. Moreover, the phosphor exhibits relative good thermal stability, the integrated emission intensity of K_2NaGaF_6:3%Mn^{4+} drops to 71.9% of the initial emission intensity at

150 °C. Finally, for proof of concept, a warm LED with CRI of 89.4, color temperature of 3779 K, luminous efficiency of 84.37 lm/W is fabricated. The fabricated LED exhibits slight color temperature and CRI change with drive current increase from 20 to 350 mA. The present work demonstrates that the K_2NaGaF_6:Mn^{4+} could be a promising red phosphor in warm WLEDs.

References

[1] T. Justel, H. Nikol and C. Ronda, Angew. Chem. Int. Edit., 1998, 37, 3085.
[2] E. F. Schubert and J. K. Kim, Science., 2005, 308, 1274.
[3] S. Pimputkar, J. S. Speck, S. P. DenBaars and S. Nakamura, Nature Photon., 2009, 3, 179.
[4] P. Pust, P. J. Schmidt and W. Schnick, Nature Mater., 2005, 18, 13.
[5] P. Pust, V. Weiler, C. Hecht, A. Tuecks, A. S. Wochnik, A. K. Henss, D. Wiechert, C. Scheu, P. J. Schmidt and W. Schnick, Nature Mater., 2014, 13, 891.
[6] R. J. Xie and N. Hirosaki, Sci Technol Adv Mat., 2007, 8, 588.
[7] C. W. Yeh, W. T. Chen, R. S. Liu, S. F. Hu, H. S. Sheu, J. M. Chen and H. T. Hintzen, J. Am. Chem. Soc., 2012, 134, 14108.
[8] C. C. Lin, A. Meijerink and R. S. Liu, J Phys Chem Lett., 2016, 7, 495.
[9] J. H. Oh, Y. J. Eo, H. C. Yoon, Y. D. Huh and Y. R. Do, J Mater Chem C., 2016, 4, 8326.
[10] H. D. Nguyen and R.S. Liu, J Mater Chem C., 2016, 4, 10759.

Journal Name

ARTICLE

[11] H. M. Zhu, C. C. Lin, W. Q. Luo, S. T. Shu, Z. G. Liu, Y. S. Liu, J. T. Kong, E. Ma, Y. G. Cao, R. S. Liu and X. Y. Chen, Nat. Commun., 2014, 5, 4312.

[12] J. H. Oh, H. Kang, Y. J. Eo, H. K. Park and Y. R. Do, J Mater Chem C., 2015, 3, 607.

[13] M. H. Fang, H. D. Nguyen, C. C. Lin and R. S. Liu, J Mater Chem C., 2015, 3, 7277.

[14] W. L. Wu, M. H. Fang, W. L. Zhou, T. Lesniewski, S. Mahlik, M. Grinberg, M. G. Brik, H. S. Sheu, B. M. Cheng, J. Wang and R. S. Liu, Chem. Mater., 2017, 29, 935.

[15] H. D. Nguyen, C. C. Lin, M. H. Fang and R. S. Liu, J Mater Chem C., 2014, 2, 10268.

[16] X. Y. Jiang, Z. Chen, S. M. Huang, J. G. Wang and Y. X. Pan, Dalton T., 2014, 43, 9414.

[17] Q. Zhou, Y. Y. Zhou, Y. Liu, L. J. Luo, Z. L. Wang, J. H. Peng, J. Yan and M. M. Wu, J Mater Chem C., 2015, 3, 3055.

[18] X. Y. Jiang, Y. X. Pan, S. M. Huang, X. A. Chen, J. G. Wang and G. K. Liu, J Mater Chem C., 2014, 2, 2301.

[19] M. Y. Peng, X. W. Yin, P. A. Tanner, M. G. Brik and P. F. Li, Chem. Mater., 2015, 27, 2938.

[20] X. Ding, G. Zhu, W. Y. Geng, Q. Wang and Y. H. Wang, Inorg. Chem., 2016, 55, 154.

[21] Y. W. Zhu, L. Huang, R. Zou, J. H. Zhang, J. B. Yu, M. M. Wu, J. Wang and Q. Su, J Mater Chem C., 2016, 4, 5690.

[22] E. H. Song, J. Q. Wang, J. H. Shi, T. T. Deng, S. Ye, M. Y. Peng, J. Wang, L. Wondraczek and Q. Y. Zhang, ACS Appl Mater Inter., 2017, 9, 8805.

[23] T. T. Deng, E. H. Song, J. Sun, L. Y. Wang, Y. Deng, S. Ye, J. Wang and Q. Y. Zhang, J Mater Chem C., 2017, 5, 2910.

[24] I. N. Flerov, M. V. Gorev, J. Grannec and A. Tressaud, J. Fluorine Chem., 2002, 116, 9.

[25] P. D. Belsare, S. V. Moharil, C. P. Joshi and S. K. Omanwar, Aip Conf Proc., 2011, 1391, 194.

[26] H. Bode, H. Jenssen and F. Bandte, Angew. Chem., 1953, 65, 304.

[27] P. Jacobs, A. Houben, W. Schweika, A. L. Tchougreeff and R. Dronskowski, J. Appl. Crystallogr., 2015, 48, 1627.

[28] S. J. Clark, M. D. Segall, C. J. Pickard, P. J. Hasnip, M. J. Probert, K. Refson and M. C. Payne, Zeitschrift Fur Kristallographie., 2005, 220, 567.

[29] J. P. Perdew, K. Burke and M. Ernzerhof, Phys. Rev. Lett., 1996, 77, 3865.

[30] D. M. Ceperley and B. J. Alder, Phys. Rev. Lett., 1980, 45, 566.

[31] J. P. Perdew and A. Zunger, Phys. Rev. B., 1981, 23, 5048.

[32] N.M. Avram and M.G. Brik, Springer and Tsinghua University Press, 2013. 2, 29.

[33] M. G. Brik and A. M. Srivastava, Opt. Mater., 2016, 54, 245.

[34] B. Z. Malkin, N. M. Abishev, E. I. Baibekov, D. S. Pytalev, K. N. Boldyrev, M. N. Popova and M. Bettinelli, Phys. Rev. B., 2017, 96, 014116.

[35] S. Schneider and R. Hoppe, Z. Anorg. Allg. Chem., 1970, 376, 268.

[36] X. Ding and Y. Wang, ACS Appl Mater Inter., 2017, 9, 23983.

[37] H.N. James, Rev. Prog. Coloration., 1985, 15, 66.

[38] T. Takahashi and S. Adachi, J. Electrochem. Soc., 2008, 155, E183.

[39] P. Rawat, S. K. Saroj, M. Gupta, G. V. Prakash and R. Nagarajan, J. Fluorine Chem., 2017, 200, 1.

[40] Y. W. Zhu, L. Y. Cao, M. G. Brik, X. J. Zhang, L. Huang, T. T. Xuan and J. Wang, J Mater Chem C., 2017, 5, 6420.

[41] L. Q. Xi, Y. X. Pan, M. M. Zhu, H. Z. Lian and J. Lin, J Mater Chem C., 2017, 5, 9255

[42] S. S. Liang, M. M. Shang, H. Lian, K. Li, Y. Zhang and J. Lin, J Mater Chem C., 2017, 5, 2927.

[43] M. Inokuti and F. Hirayama, J. Chem. Phys., 1965, 43, 1978.

[44] H. Chen, H. Lin, Q. Huang, F. Huang, J. Xu, B. Wang, Z. Lin, J. Zhou and Y. Wang, J Mater Chem C., 2016, 4, 2374.

[45] C. W. Struck and W. H. Fonger, J. Appl. Phys., 1971, 42, 4515.

[46] M. M. Zhu, Y. X. Pan, L. Q. Xi, H. Z. Lian and J. Lin, J Mater Chem C., 2017, 5, 10241.

[47] T. Hu, H. Lin, Y. Cheng, Q. M. Huang, J. Xu, Y. Gao, J. M. Wang and Y. S. Wang, J Mater Chem C., 2017, 5, 10241

[48] X. J. Zhang, Y. T. Tsai, S. M. Wu, Y. C. Lin, J. F. Lee, H. S. Sheu, B. M. Cheng and R. S. Liu, ACS Appl Mater Inter., 2016, 8, 19612.